

## REFERENCES

1. Pike CP. Imaging of inflammatory sites in the 1990s: new horizons [Editorial]. *J Nucl Med* 1991;32:2034–2036.
2. Datz FL, Morton KA. New radiopharmaceuticals for detecting infection. *Invest Radiol* 1993;28:356–365.
3. Fischman AJ, Rubin RH, Khaw BA, et al. Detection of acute inflammation with <sup>111</sup>In-labeled nonspecific polyclonal IgG. *Semin Nucl Med* 1988;18:335–344.
4. Oyen WJG, Claessens RAMJ, van der Meer JWM, Corstens FHM. Detection of subacute infectious foci with indium-111-labeled autologous leukocyte and indium-111-labeled human nonspecific immunoglobulin G: a prospective, comparative study. *J Nucl Med* 1991;32:1854–1860.
5. Corstens FHM, van der Meer JWM. Imaging inflammation with human polyclonal immunoglobulin: not looked for but discovered [Editorial]. *Eur J Nucl Med* 1992;19:155–158.
6. Boerman OC, Storm G, Oyen WJG, et al. Sterically stabilized liposomes labeled with <sup>111</sup>In to image focal infection. *J Nucl Med* 1995;36:1639–1644.
7. Babich JW, Solomon H, Pike MC, et al. Technetium-99m-labeled hydrazino nicotinamide derivatized chemotactic peptide analogs for imaging focal sites of bacterial infection. *J Nucl Med* 1993;34:1964–1974.
8. Corstens FHM, van der Meer JWM. Chemotactic peptides: new locomotion for imaging of infection? [Editorial]. *J Nucl Med* 1991;32:491–494.
9. Moyer BR, Vallabhajosula S, Lister-James J, et al. Development of a white blood cell specific technetium-99m imaging agent from platelet factor 4 for detecting infection. *J Nucl Med* 1996;37:673–679.
10. Subramanian R, Colony J, Shaban S, et al. New chelating agent for attaching indium-111 to monoclonal antibodies: in vitro and in vivo evaluation. *Bioconjugate Chemistry* 1992;3:248–256.
11. Klein JL, DeJager RL, Stiekema JCJ, et al. Human monoclonal antibodies. Application in radioimmunotherapy. In: Goldenberg DM, ed. *Cancer therapy with radiolabeled antibodies*. Boca Raton, FL: CRC Press; 1995:271–281.
12. Vallabhajosula S, Subramanian R, Palestro CJ, et al. Evaluation of indium-111-labeled immunoglobulins for imaging infection: IgM versus IgG antibodies. *J Nucl Med* 1992;33:1031.
13. Oyen WJG, Boerman OC, et al. Biodistribution of indium-111-labeled IgG and IgM in experimental infection. *Nucl Med Commun* 1996;17:616–620.
14. Vallabhajosula S, Subramanian R, Zhao QH, et al. Indium-111-LiLo-human monoclonal IgM 16.88, a new tracer for imaging focal infection: comparison of kinetics with indium-111-polyclonal IgG. *Eur J Nucl Med* 1995;22:903.
15. Haspel MV, McCabe RP, Pomato N, et al. Generation of tumor cell reactive human monoclonal antibodies using peripheral blood lymphocytes from actively immunized colorectal carcinoma patients. *Cancer Res* 1985;45:3951–3961.
16. Peters LC, Brandhorst JS, Hanna MG Jr. Preparation of immunotherapeutic autologous tumor cell vaccines from solid tumors. *Cancer Res* 1979;39:1353–1360.
17. Pomato N, Murray JH, Bos E, Haspel MV, McCabe RP, Hanna MG Jr. Identification and characterization of a human colon tumor-associated antigen, CTAA-16.88, recognized by a human monoclonal antibody. In: Metzgar RS, Mitchell MS, eds. *Human tumor antigens and specific tumor therapy*. New York, NY: Alan R. Liss; 1989:127–136.
18. Subramanian R, Meares CF. Bifunctional chelating agents for radiometal-labeled monoclonal antibodies. In: Goldenberg DM, ed. *Cancer imaging with radiolabeled antibodies*. Boston: Kluwer Academic; 1990:183–199.
19. Sell S. *Immunology immunopathology and immunity*, 4th ed. New York: Elsevier; 1987.
20. McCabe RP, Haspel MV, Carrasquillo JA, et al. Recent developments and perspectives on the future of human and murine monoclonal antibodies in the diagnosis and treatment of cancer. In: Crommelin DJA, Schellekens H, eds. *From clone to clinic*. Amsterdam: Kluwer; 1990:175–188.
21. Steis RG, Carrasquillo JA, Bookman MA, et al. Toxicity, immunogenicity and tumor radioimmunodetecting ability of two human monoclonal antibodies in patients with metastatic colorectal carcinoma. *J Clin Oncol* 1990;8:476–490.
22. Subramanian R, Klein JL, Williams JR, Song S-Y, Hanna MG Jr. Yttrium-90-labeled human monoclonal antibodies for radioimmunotherapy-preclinical evaluation in rabbits. *Proceedings of the American Association for Cancer Research* 1994;35:527.
23. Halpern SE, Hagen PL, Chen A, et al. Distribution of radiolabeled human and mouse monoclonal IgM antibodies in murine models. *J Nucl Med* 1988;29:1688–1696.
24. Vallabhajosula V, Ali KSM, Goldsmith SJ, et al. Evaluation of technetium-99m-labeled peptides for imaging infection in a rabbit model [Abstract]. *J Nucl Med* 1993;34(suppl):104P.
25. Taddei-Peters WC, Haspel MV, Vente P, et al. Quantitation of human tumor-reactive monoclonal antibody 16.88 in the circulation and localization of 16.88 in colorectal metastatic tumor tissue using murine antiidiotypic antibodies. *Cancer Res* 1992;52:2603–2609.
26. Haisma HJ, Pinedo HM, Dessel, MAP, et al. Human IgM monoclonal antibody 16.88: pharmacokinetics and immunogenicity in colorectal cancer patients. *J Natl Cancer Inst* 1991;83:1813–1819.
27. Klein JL, DeJager RL, McCullers GA, Stiekema JCJ, Subramanian R, Hanna MG Jr. Human antihuman antibody response (HAHA) to injection of <sup>99m</sup>Tc-, <sup>131</sup>I- and <sup>90</sup>Y-labeled human monoclonal antibody. *J Immunother* 1994;16:168.

---

# Three-Dimensional Dosimetry for Intralesional Radionuclide Therapy Using Mathematical Modeling and Multimodality Imaging

Glenn D. Flux, Steve Webb, Robert J. Ott, Sarah J. Chittenden and Robert Thomas

Joint Department of Physics, Institute of Cancer Research and Royal Marsden National Health Service Trust, Downs Road, Sutton, Surrey, SM2 5PT, United Kingdom

---

A method of dosimetry is described that quantifies the three-dimensional absorbed-dose distribution resulting from an intralesional administration of a radiolabeled monoclonal antibody, allowing for both spatial and temporal heterogeneity of distribution of the radionuclide and without the need for a calibration scan. **Methods:** A mathematical model was developed to describe the distribution of activity as a function of time resulting from infusion at a single point within the solid component of a tumor. The parameters required for this model are either known directly or may be obtained from SPECT image data registered to computed tomography. Convolution of this distribution with a point-source dose kernel enabled the three-dimensional absorbed-dose distribution to be obtained. **Results:** This method was applied to a set of patient data acquired in the course of a clinical study performed at our center, and dose profiles and dose-volume histograms were produced. It was shown that the

three-dimensional distribution of dose was significantly nonuniform. **Conclusion:** Initial results suggest that this method offers a means of determining the absorbed dose distribution within a tumor resulting from intralesional infusion. This method extends the Medical Internal Radiation Dose computation, which, in these circumstances, would make erroneous assumptions. Furthermore, it will enable individual patient treatment planning and optimization of the parameters that are within the clinician's control.

**Key Words:** dosimetry; image registration; glioma; radioimmunotherapy; intralesional therapy

**J Nucl Med** 1997; 38:1059–1066

---

**T**argeted radionuclide therapy, using radiolabeled monoclonal antibodies (MAbs), aims to deliver a therapeutic dose to a tumor while minimizing the dose to nontarget organs. It has been shown that intralesional therapy, whereby the radiopharmaceutical is administered directly into the tumor by means of an

---

Received May 13, 1996; revision accepted Nov. 23, 1996.

For correspondence or reprints contact: Glenn D. Flux, Joint Department of Physics, Royal Marsden National Health Service Trust, Downs Road, Sutton, Surrey, SM2 5PT, United Kingdom.

indwelling catheter, can significantly increase the uptake as compared with intravenous or intra-arterial administration (1).

The feasibility of intralesional radionuclide therapy to treat recurrent high-grade glioma was determined in a clinical trial performed at the Royal Marsden National Health Service Trust. In this trial, up to 650 MBq of  $^{131}\text{I}$ -conjugated MAb was administered directly, at a rate of 100  $\mu\text{l/hr}$ , by means of an indwelling catheter inserted stereotactically into the solid component of the tumor. An x-ray CT scan was taken before the insertion of the catheter with the patient wearing a stereotactic head frame and localization device. This scan was used to determine the correct trajectory and position for the needle and also to delineate tumor volume and anatomical features. After administration of the radiopharmaceutical, a series of SPECT scans were obtained to monitor the distribution of the activity. Magnetic resonance imaging and  $^{18}\text{F}$ -deoxyglucose PET scans were also obtained in some cases to aid in delineating the tumor volume and surrounding anatomy. All scans were registered using a point-based technique on external markers attached to reproducible positions on the skull of the patient. These markers consisted of perspex disks containing a hollow sphere into which was inserted a substance suitable for the imaging modality—barium sulfate for CT, gadolinium for magnetic resonance imaging,  $^{68}\text{Ge}$  for PET and  $^{99\text{m}}\text{Tc}$  for SPECT. In the latter case, dual-energy windows were used to obtain simultaneously separate three-dimensional image sets of the markers and the  $^{131}\text{I}$  image data, which were therefore automatically registered. In all cases, the series of SPECT scans demonstrated that transport of the labeled MAb through the tumor had ceased before the time of the first scan.

The conventional Medical Internal Radiation Dose (MIRD) approach to the determination of absorbed dose provides only a mean dose for a given target volume due to some source-target configuration and relies on several approximations. In particular, the assumption is made that the activity is uniformly distributed throughout the source organ (2,3). In the specific case of intralesional therapy, all radiolabeled activity diffuses from a point (or points) within the tumor. Depending on the diffusion characteristics of the antibody within the tumor tissue, this can lead to a heterogeneous distribution of activity and hence of absorbed dose. Thus, whereas an average dose value may indicate a significant therapeutic effect, it is possible that a large volume of the tumor receives only a negligible dose. This would translate into a very low probability of tumor control (4). Therefore, there is a need for greater accuracy in determining the spatial variation in absorbed dose from infusion of a therapeutic level of activity.

Several authors have used registered functional and anatomical image data as a basis for determining three-dimensional dosimetry (5–8). In this method, the imaged activity distribution is convolved with the relevant point-source dose kernel (generated using Monte Carlo techniques) to obtain the absorbed three-dimensional dose distribution. This “image-based” approach to dosimetry allows for spatial variation of activity and results in the determination of a heterogeneous dose distribution, a significant improvement on the MIRD system. It is not possible using this approach, however, to incorporate temporal variation in the activity distribution, which, as we shall show in this paper, has a significant bearing on the resulting dose distribution. In addition, this technique relies on a calibration scan to quantify the activity distribution, thus introducing further potential sources of error.

With this in mind, a method has been developed to quantify the three-dimensional dose distribution resulting from an intralesional infusion of activity, allowing for both spatial and

temporal heterogeneity of the activity distribution. This method uses a combination of mathematical modeling, multimodality imaging and three-dimensional image registration. By considering the amount of activity injected and the duration of infusion, and by estimating the effective half-life of the isotope and the rate of diffusion of the MAb through the tumor, an expression was obtained, subject to several assumptions, which gave the concentration of activity at any point within the lesion at any given time after the commencement of infusion. The distribution of the total number of radioactive decays as a function of distance from the source (i.e., the point at which the activity is introduced) was obtained by integrating this expression over time. This function was then convolved with the relevant point-source dose kernel to produce a three-dimensional dose distribution, which accounted for both spatial and temporal distribution of the radionuclide. Registration of SPECT and CT image data enabled the distribution within the tumor to be ascertained and visualized and dose-volume histograms (DVHs) to be determined.

In this paper, a mathematical model is presented that leads to a derivation of the distribution of activity over the whole time-course of irradiation. Initially, the assumptions were made that: (a) there is a single phase of decay and (b) the activity diffuses at a constant and continuous rate. Further modifications were then made to deal with both of these assumptions in order to apply this method to data obtained in the course of a clinical trial performed at the Royal Marsden National Health Service Trust, to treat recurrent high-grade glioma. These modifications allow for a two-phase decay process and incorporate cessation of diffusion at some time after infusion.

## MATERIALS AND METHODS

### Derivation of the Decay Distribution Equation

This model aims to determine the total number of decays occurring at a point a distance  $r$  from the point of infusion of activity. The derivation was broken down into several steps in which the assumptions become increasingly less general and more closely model the real situation.

### Instantaneous Infusion of Activity at a Point ( $r = 0$ )

In this case, the concentration of activity at a point a distance  $r$  from the source, at a time  $t$  after infusion, ignoring decay, is given by Crank (9):

$$C(r, t) = \frac{M}{8(\pi\kappa t)^{3/2}} \left[ \exp\left(\frac{-r^2}{4\kappa t}\right) \right], \quad \text{Eq. 1}$$

where  $C(r, t)$  is the concentration of activity (in  $\text{MBq cm}^{-3}$ ),  $M$  is the total amount of activity within the volume (in MBq) and  $\kappa$  is the diffusion constant (in  $\text{cm}^2\text{h}^{-1}$ ).

The transport of the antibody through tissue, and its removal, is dependent on several processes including convection, antigen binding and the vasculature. It is not possible, however, to isolate the individual effects of these factors from the image data. Therefore, the term “diffusion” is used loosely throughout to encompass all forms of transport. This equation assumes radial diffusion within an infinite volume so that no boundary conditions were considered, such as reflection or an abrupt change in the medium. This is a reasonable assumption for the present problem, since brain may be treated as solid water of unit density, and registered image data showed that the activity did not measurably reflect at the boundary of the tumor.

Incorporating monoexponential decay, the total amount of activity at time  $t$  is

$$M(t) = M_0 e^{-\lambda t}, \quad \text{Eq. 2}$$

where  $M_0$  is the total amount of activity at time  $t = 0$  (in MBq), and  $\lambda_e$  is the effective decay constant (in  $h^{-1}$ ), which accounts for biological clearance ( $\lambda_{biol}$ ), as well as physical decay ( $\lambda_{phys}$ ) (i.e.,  $\lambda_e = \lambda_{phys} + \lambda_{biol}$ ).

Thus, incorporating effective decay, Equation 1 becomes

$$C(r, t) = \frac{M_0}{8(\pi\kappa)^{3/2}} \left[ \exp - \left( \frac{r^2}{4\kappa t} + \lambda_e t \right) \right]. \quad \text{Eq. 3}$$

This expression is accurate only where the rate of infusion is high compared with the rate of diffusion, which may not hold true. It is therefore necessary to consider the effect on the distribution of a gradual infusion, and this modification is made next.

#### Constant and Continuous Infusion at a Point ( $r = 0$ )

In this case, the total activity at time  $t$  within the volume, excluding decay, is

$$M(t) = \varphi(t) \times t, \quad \text{Eq. 4}$$

where  $\varphi(t)$  is the rate of infusion of the activity (in MBq  $h^{-1}$ ).

The exponential decay of the activity  $\varphi(t)$  takes the form

$$\varphi(t) = Q_0 e^{-\lambda_p t}, \quad \text{Eq. 5}$$

where  $Q_0$  is the initial rate of infusion of activity (in MBq  $h^{-1}$ ), and  $\lambda_p$  is the physical decay constant of the isotope (in  $h^{-1}$ ).

The elemental concentration  $dC(r, t)$  from an elemental infusion  $\varphi(t')dt'$  in time  $dt'$  is, by analogy with Equation 3

$$dC(r, t) = \frac{Q_0 e^{-\lambda_p t'} dt'}{8(\pi\kappa)^{3/2} (t - t')^{3/2}} \left[ \exp \left( \frac{-r^2}{4\pi(t - t')} \right) \right] e^{-\lambda_e(t-t')}, \quad \text{Eq. 6}$$

where the factor  $e^{-\lambda_e(t - t')}$  is introduced to allow for decay after infusion. To obtain the total concentration,  $C(r, t)$  was integrated, this being considerably simplified by making the assumption that

$$\lambda_p \sim \lambda_e \quad \text{Eq. 7}$$

for the duration of the infusion so that

$$e^{(\lambda_e - \lambda_p)t'} \sim 1. \quad \text{Eq. 8}$$

While this assumption may have a significant bearing on final results in the case of continuous infusion, in reality infusion only occurs for a finite time. The model has been adapted accordingly in the next section.

The total concentration from continuous infusion from time 0 to time  $t$  is thus

$$C(r, t) = \frac{Q_0 e^{-\lambda_e t}}{8(\pi\kappa)^{3/2}} \int_0^t \exp \left[ \frac{-r^2}{4\kappa(t - t')} \right] \frac{dt'}{(t - t')^{3/2}} \quad \text{Eq. 9}$$

so that

$$C(r, t) = Q_0 \frac{e^{-\lambda_e t}}{4\pi\kappa r} \operatorname{erfc} \left( \frac{r}{2(\kappa t)^{1/2}} \right) \quad \text{Eq. 10}$$

where  $\operatorname{erfc}(\rho)$  is the complementary error function defined as

$$\operatorname{erfc}(\rho) = 1 - \operatorname{erf}(\rho) = 1 - \frac{2}{\sqrt{\pi}} \int_0^\rho e^{-\zeta^2} d\zeta. \quad \text{Eq. 11}$$

Equation 10 gives the concentration of activity at a point a distance  $r$  from the source of infusion at a time  $t$  from the commencement of infusion, if the infusion rate is constant until this time. This was the case in the clinical study reported.

#### Infusion for a Finite Time at a Constant Rate at a Point ( $r = 0$ )

The next step was to determine the concentration at time  $t$  if the infusion ceases at time  $t_f$ . In this case, Equation 9 was amended to integrate only as far as time  $t_f$ , i.e.,

$$C(r, t) = \frac{Q_0 e^{-\lambda_e t}}{8(\pi\kappa)^{3/2}} \int_0^{t_f} \exp \left[ \frac{-r^2}{4\kappa(t - t')} \right] \frac{dt'}{(t - t')^{3/2}}, \quad \text{Eq. 12}$$

which gives

$$C(r, t) = \frac{Q_0 e^{-\lambda_e t}}{4\pi\kappa r} \left[ \operatorname{erfc} \left( \frac{r}{2(\kappa t)^{1/2}} \right) - \operatorname{erfc} \left( \frac{r}{2[\kappa(t - t_f)]^{1/2}} \right) \right] \quad \text{Eq. 13}$$

( $t > t_f$ ).

Thus, the concentration of activity at a point a distance  $r$  from the source, at time  $t$  from the commencement of infusion, due to infusion of activity at an initial rate  $Q_0$ , for a duration  $t_f$ , is given by

$$C(r, t) = \frac{Q_0 e^{-\lambda_e t}}{4\pi\kappa r} \left[ \operatorname{erfc} \left( \frac{r}{2(\kappa t)^{1/2}} \right) - H(t - t_f) \operatorname{erfc} \left( \frac{r}{2[\kappa(t - t_f)]^{1/2}} \right) \right], \quad \text{Eq. 14}$$

where  $H(t - t_f)$  is the Heaviside unit step function, i.e.,

$$H(t - t_f) = \begin{cases} 0 & t < t_f \\ 1 & t \geq t_f \end{cases} \quad \text{Eq. 15}$$

Note that Equation 14 subsumes the earlier case of Equation 10.

#### Total Decay Concentration Distribution

Equation 14 was integrated over time to obtain the concentration of the total number of decays occurring at any given point a distance  $r$  from the source, i.e.,

$$N(r) = \frac{Q_0}{4\pi\kappa r} \left[ \int_0^\infty e^{-\lambda_e t} \operatorname{erfc} \left( \frac{r}{2(\kappa t)^{1/2}} \right) dt - \int_{t_f}^\infty e^{-\lambda_e t} \operatorname{erfc} \left( \frac{r}{2[\kappa(t - t_f)]^{1/2}} \right) dt \right], \quad \text{Eq. 16}$$

which has the solution

$$N(r) = \frac{Q_0 \exp[-r(\lambda_e/\kappa)^{1/2}]}{4\pi\kappa\lambda_e r} (1 - e^{-\lambda_e t_f}), \quad \text{Eq. 17}$$

where  $N(r)$  has dimensions  $cm^{-3}$ . It is interesting to note here that the clinician only has control over two of the parameters in this model—the initial rate of activity infused ( $Q_0$ ) and the duration of infusion ( $t_f$ ). It may be seen from Equation 14 that the distribution of the concentration of decays at any given time after infusion is influenced by the duration of infusion. From Equation 17, however, it is evident that distribution of the *summed* concentration of decays is not affected by either of these factors. Thus, for any given isotope and medium throughout which diffusion occurs, there is no control over the decay distribution and consequently over the distribution of absorbed dose throughout the tumor. The dose may only be increased at the periphery of a tumor at the expense of a corresponding increase in dose values closer to the source point.

#### Modification to Incorporate Cessation of Diffusion

In the clinical study to which this method was applied it was found that diffusion did not continue at a constant rate but in fact ceased

altogether. The mechanisms for this are not well understood, although it was speculated that either all the MAb was bound to sites close to the infusion point or that the size of the MAb molecule hindered its progress through the tumor tissue. It is probable that the rate of transport of the MAb gradually ceases. This will give rise to a complex function that may not be directly determined. It is profitable, however, to incorporate into the model the possibility that diffusion ceases abruptly at some time  $t_D$  after the commencement of infusion. This closely follows the derivation of Equation 17 to describe the dose distribution for continuous diffusion.

In the case of instantaneous infusion, the concentration of activity at a distance  $r$  from the source, at time  $t$  after the start of infusion, is

$$C(r, t) = \begin{cases} \frac{M_0}{8(\pi\kappa t)^{3/2}} \exp[-(r^2/4\kappa t + \lambda_c t)] & (t_D > t) \\ \frac{M}{8(\pi\kappa t_D)^{3/2}} \exp[-(r^2/4\kappa t_D + \lambda_c t)] & (t \geq t_D) \end{cases}, \text{ Eq. 18}$$

where  $t_D$  is the time at which diffusion ceases and  $M_0$  is the amount of activity just before infusion.

For infusion at a constant rate for a finite time,  $t_r$ , we therefore obtain, when  $t \geq t_D$ ,

$$C(r, t) = \frac{Q_0 e^{-\lambda_c t}}{8(\pi\kappa)^{3/2}} \int_0^{t_r} \exp(-r^2/4\kappa(t_D - t')) \frac{dt'}{(t_D - t')^{3/2}} \quad \text{Eq. 19}$$

$$(t \geq t_D > t_r),$$

which leads to

$$C(r, t) = \frac{Q_0 e^{-\lambda_c t}}{4\pi\kappa r} \left[ \operatorname{erfc}\left(\frac{r}{2(\kappa t_D)^{1/2}}\right) - \operatorname{erfc}\left(\frac{r}{2[\kappa(t_D - t_r)]^{1/2}}\right) \right] \quad \text{Eq. 20}$$

$$(t \geq t_D > t_r).$$

It is assumed in the model that  $t_D \geq t_r$ , and this was observed clinically. The full expression for the concentration of activity at any time after the commencement of infusion must incorporate terms for  $t < t_D$  that have been obtained previously:

$$C(r, t) = \begin{cases} \frac{Q_0 e^{-\lambda_c t}}{4\pi\kappa r} \left[ \operatorname{erfc}\left(\frac{r}{2(\kappa t)^{1/2}}\right) \right] & (t_D > t_r \geq t) \\ \frac{Q_0 e^{-\lambda_c t}}{4\pi\kappa r} \left[ \operatorname{erfc}\left(\frac{r}{2(\kappa t)^{1/2}}\right) - \operatorname{erfc}\left(\frac{r}{2[\kappa(t - t_r)]^{1/2}}\right) \right] & (t_D > t > t_r) \\ \frac{Q_0 e^{-\lambda_c t}}{4\pi\kappa r} \left[ \operatorname{erfc}\left(\frac{r}{2(\kappa t_D)^{1/2}}\right) - \operatorname{erfc}\left(\frac{r}{2[\kappa(t_D - t_r)]^{1/2}}\right) \right] & (t \geq t_D > t_r) \end{cases}$$

$$\text{Eq. 21}$$

To obtain the total concentration of decays at a point  $N(r)$ , it was necessary to integrate this equation over time, with appropriate limits, i.e.,

$$N(r) = \frac{Q_0}{4\pi\kappa r} \left\{ \int_0^{t_r} e^{-\lambda_c t} \operatorname{erfc}\left(\frac{r}{2(\kappa t)^{1/2}}\right) dt + \int_{t_r}^{t_D} e^{-\lambda_c t} \operatorname{erfc}\left(\frac{r}{2(\kappa t)^{1/2}}\right) dt \right.$$

$$\left. - \int_{t_r}^{t_D} e^{-\lambda_c t} \operatorname{erfc}\left(\frac{r}{2[\kappa(t - t_r)]^{1/2}}\right) dt + \int_{t_D}^{\infty} e^{-\lambda_c t} \operatorname{erfc}\left(\frac{r}{2(\kappa t_D)^{1/2}}\right) dt - \int_{t_D}^{\infty} e^{-\lambda_c t} \operatorname{erfc}\left(\frac{r}{2[\kappa(t_D - t_r)]^{1/2}}\right) dt \right\}. \quad \text{Eq. 22}$$

This was integrated to give

$$N(r) = \frac{Q_0 e^{-\lambda_c t_D}}{4\pi\kappa r} \left[ \operatorname{erfc}\left(\frac{r}{2(\kappa t_D)^{1/2}}\right) - \operatorname{erfc}\left(\frac{r}{2[\kappa(t_D - t_r)]^{1/2}}\right) \right] + \frac{Q_0}{4\pi\kappa r} \left\{ \int_0^{t_D} e^{-\lambda_c t} \operatorname{erfc}\left(\frac{r}{2(\kappa t)^{1/2}}\right) dt - e^{-\lambda_c t_D} \int_0^{(t_D - t_r)} e^{-\lambda_c t} \operatorname{erfc}\left(\frac{r}{2(\kappa t)^{1/2}}\right) dt \right\}. \quad \text{Eq. 23}$$

This equation was integrated numerically to give the total concentration of decays at any point, since the two contributing integrals cannot be analytically reduced.

#### Modification to Allow for Two-Phase Decay

Following infusion, the transport of the radiolabeled antibody follows a complex pattern. While some of the antibody remains within the tumor, bound or unbound to the target protein, a substantial portion of it may reach blood vessels and be washed out or may even be redeposited within the tumor itself. The concentration of the activity will be affected by all of these factors. In practice, this may result in a two-phase decay process apparent in some patient data. A commonplace and accurate approximation made here is to consider both phases as exponential (10). This results in an initial effective decay rate that will be greater than the second. Both values can make a significant contribution to the calculation of the dose distribution. The point from which the second phase dominates,  $t_x$ , however, is frequently sharply defined so that it is necessary only to consider the effect of constant decay values occurring consecutively, rather than to assess the case for a variable decay coefficient. In the clinical study considered here, it was found that  $t_x > t_D$ .

Consider the decay concentration,  $C(r, t)$ , as a function of time, in the case of two consecutively occurring decay rates, governed by  $\lambda_a$  and  $\lambda_b$  (Fig. 1).

In both phases the decay distribution equation may be approximated to be an exponential, i.e., for  $t_x \geq t > t_D$

$$C(r, t) = \alpha e^{-\lambda_a t} \quad \text{Eq. 24}$$

for some constant  $\alpha$ . Similarly, for  $t \geq t_x > t_D$

$$C(r, t) = \beta e^{-\lambda_b t} \quad \text{Eq. 25}$$

for some constant  $\beta$ .

Equating Equations 24 and 25 at time  $t_x$  and substituting for  $\alpha$  in Equations 25 and 20 gives

$$\beta = \frac{Q_0 e^{t_x(\lambda_b - \lambda_a)}}{4\pi\kappa r} \left[ \operatorname{erfc}\left(\frac{r}{2(\kappa t_D)^{1/2}}\right) - \operatorname{erfc}\left(\frac{r}{2[\kappa(t_D - t_r)]^{1/2}}\right) \right]. \quad \text{Eq. 26}$$

Thus, for  $t = t_x$ , the decay concentration equation was obtained from Equation 25. There are now four separate terms for this

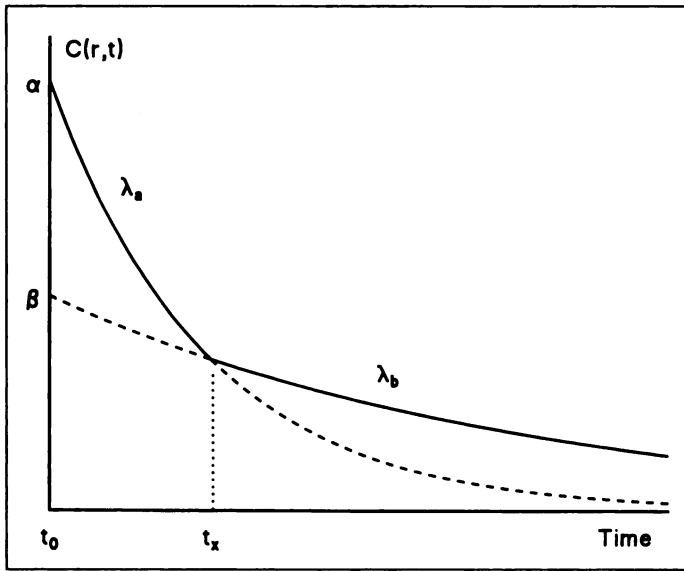


**FIGURE 1.** Two-phase decay. The solid line indicates the actual decay concentration value at an arbitrary point  $r$  as a function of time, where the decay may be considered as being governed by two consecutive decay constants  $\lambda_a$  and  $\lambda_b$ . The time at which the second decay rate dominates is marked here as  $t_x$ .

concentration value, each pertaining to a particular phase of the infusion, diffusion and decay, i.e.,

$$C(r, t) = \begin{cases} \frac{Q_0 e^{-\lambda_a t}}{4\pi\kappa r} \left[ \operatorname{erfc} \left( \frac{r}{2(\kappa t)^{1/2}} \right) \right] & (t_x > t_D > t_f \geq t) \\ \frac{Q_0 e^{-\lambda_a t}}{4\pi\kappa r} \left[ \operatorname{erfc} \left( \frac{r}{2(\kappa t)^{1/2}} \right) - \operatorname{erfc} \left( \frac{r}{2[\kappa(t - t_f)]^{1/2}} \right) \right] & (t_x > t_D > t > t_f) \\ \frac{Q_0 e^{-\lambda_a t}}{4\pi\kappa r} \left[ \operatorname{erfc} \left( \frac{r}{2(\kappa t_D)^{1/2}} \right) - \operatorname{erfc} \left( \frac{r}{2[\kappa(t_D - t_f)]^{1/2}} \right) \right] & (t_x > t \geq t_D > t_f) \\ \frac{Q_0 e^{-\lambda_a t} e^{-(\lambda_b - \lambda_a)t_x}}{4\pi\kappa r} \left[ \operatorname{erfc} \left( \frac{r}{2(\kappa t_D)^{1/2}} \right) - \operatorname{erfc} \left( \frac{r}{2[\kappa(t_D - t_f)]^{1/2}} \right) \right] & (t > t_x \geq t_D > t_f). \end{cases}$$

Eq. 27

Therefore, to obtain the total decay distribution equation analogous to Equation 23 for the simpler case, it was necessary to integrate over all of these terms. This gives

$$N(r) = \frac{Q_0}{4\pi\kappa r} \left\{ \left[ \operatorname{erfc} \left( \frac{r}{2(\kappa t_D)^{1/2}} \right) - \operatorname{erfc} \left( \frac{r}{2[\kappa(t_D - t_f)]^{1/2}} \right) \right] \cdot \left( \frac{e^{-\lambda_a t_D}}{\lambda_a} - \frac{e^{-\lambda_a t_x}}{\lambda_a} - \frac{e^{-\lambda_a t_x}}{\lambda_b} \right) + \int_0^{t_D} e^{-\lambda_a t} \operatorname{erfc} \left( \frac{r}{2(\kappa t)^{1/2}} \right) dt - e^{-\lambda_a t_f} \int_0^{t_D - t_f} e^{-\lambda_a t} \operatorname{erfc} \left( \frac{r}{2(\kappa t)^{1/2}} \right) dt \right\}.$$

Eq. 28

This equation requires numerical evaluation. Equation 28 is the full expression for the number of decays  $N(r)$  at radius  $r$ , when an

activity  $Q_0$  is infused for time  $t_f$  at constant rate, diffuses at constant rate until time  $t_D$  and decays with two effective decay constants  $\lambda_a$  and  $\lambda_b$ , changing slope at time  $t_x$ . The model requires that  $t_x > t_D > t_f$ .

### Parameters Required by the Model

Of the parameters involved here, two are known directly, whereas others must be inferred from the image data. The initial rate of infusion,  $Q_0$ , and the duration of infusion,  $t_f$ , are both known directly.

The effective decay constants within the region of interest,  $\lambda_a$  and  $\lambda_b$ , are the sum of the physical and biological decay constants and may be directly determined if two or more SPECT scans for the same patient have been obtained, for each phase, with identical set-up parameters and registered with anatomical CT data on which the clinician has outlined the tumor volume. By transferring these contours to the functional data, the voxel activity values within the tumor may be summed for each SPECT image set. It is then possible to use the property that, although diffusion rearranges the activity, the total imaged activity changes only due to the effective decay. Thus, for  $m$  voxels within a tumor volume,

$$A(t_n) = \sum_{i=1}^m V_i(t_n), \quad \text{Eq. 29}$$

where  $A(t_n)$  is the total imaged activity within the tumor at time  $t_n$ , and  $V_i$  is the activity value of the  $i$ th voxel.

For two scans, taken at times  $t_{n-1}$  and  $t_n$ , we have

$$A(t_n) = A(t_{n-1}) e^{-\lambda_n(t_n - t_{n-1})}, \quad \text{Eq. 30}$$

which was rearranged to obtain

$$\lambda_n = \frac{1}{t_n - t_{n-1}} [\ln A(t_{n-1}) - \ln A(t_n)]. \quad \text{Eq. 31}$$

For  $M$  image sets,  $(M - 1)$  values of  $\lambda_n$  were obtained, from which a mean was calculated. It was in this process that the two separate constants  $\lambda_a$  and  $\lambda_b$  were determined.

### Determination of the Diffusion Constant

The distribution of the concentration of activity as imaged by the gamma camera,  $C_\gamma$ , should, apart from a constant, approximate Equation 27, for example:

$$C_\gamma(r, t) = \frac{KQ_0 e^{-\lambda_a t}}{4\pi\kappa r} \left[ \operatorname{erfc} \left( \frac{r}{2(\kappa t_D)^{1/2}} \right) - \operatorname{erfc} \left( \frac{r}{2[\kappa(t_D - t_f)]^{1/2}} \right) \right] \quad \text{Eq. 32}$$

( $t_x > t \geq t_D > t_f$ ),

where  $K$  is a (dimensionless) calibration factor relating voxel values directly to absolute activity.

A maximum value for any scan was obtained by considering that the maximum concentration of decays will occur at  $r = 0$ , the point of infusion. From Equation 32:

$$C_{\gamma_{\max}}(t) = C_\gamma(0, t) = \frac{KQ_0 e^{-\lambda_a t}}{4\pi\kappa} \lim_{r \rightarrow 0} \left\{ \frac{1}{r} \left[ \operatorname{erf} \left( \frac{r}{2[\kappa(t_D - t_f)]^{1/2}} \right) - \operatorname{erf} \left( \frac{r}{2(\kappa t_D)^{1/2}} \right) \right] \right\}$$

Eq. 33

( $t_x > t \geq t_D > t_f$ )

$$= \frac{KQ_0e^{-\lambda t}}{4(\pi\kappa)^{3/2}} \left[ \frac{1}{(t_D - t_f)^{1/2}} - \frac{1}{t_D^{1/2}} \right]. \quad \text{Eq. 34}$$

A value for the  $1/n$ th maximum decay concentration value was obtained from both Equations 32 and 34. Equating these gives

$$\frac{KQ_0e^{-\lambda t}}{4n(\pi\kappa)^{3/2}} \left[ \frac{1}{(t_D - t_f)^{1/2}} - \frac{1}{t_D^{1/2}} \right] = \frac{KQ_0e^{-\lambda t}}{4\pi\kappa r_n} \left[ \operatorname{erfc} \left( \frac{r_n}{2(\kappa t_D)^{1/2}} \right) - \operatorname{erfc} \left( \frac{r_n}{2[\kappa(t_D - t_f)]^{1/2}} \right) \right], \quad \text{Eq. 35}$$

where  $r_n$  is the  $(1/n)$ th width of the image activity profile such that

$$C_\gamma(r_n, t) = \frac{C_{\gamma\max}}{n}. \quad \text{Eq. 36}$$

The constants  $Q_0$ ,  $\lambda_a$  and most importantly  $K$  were eliminated leaving

$$\frac{1}{(t_D - t_f)^{1/2}} - \frac{1}{t_D^{1/2}} = \frac{n(\pi\kappa)^{1/2}}{r_n} \left[ \operatorname{erfc} \left( \frac{r_n}{2(\kappa t_D)^{1/2}} \right) - \operatorname{erfc} \left( \frac{r_n}{2[\kappa(t_D - t_f)]^{1/2}} \right) \right]. \quad \text{Eq. 37}$$

Of the parameters involved here,  $t_f$  was known,  $t_D$  was estimated and  $r_n$  was directly measured from the image data. By solving this equation numerically, a mean value of  $\kappa$  was obtained from SPECT scans acquired for times ( $t_x > t \geq t_D > t_f$ ). While the example given here is for a time that is relevant to the clinical study, a similar procedure will work for the cases (a) ( $t_x > t_D > t > t_f$ ) and (b) ( $t > t_x \geq t_D > t_f$ ).

### Dose Calculation Algorithm

Convolving the total decay distribution Equation 28 with the point-source dose kernel for the radionuclide enables an accurate approach to be made in determining the three-dimensional dose distribution to the target volume. To obtain a quantitative dose distribution, giving absolute rather than relative values of absorbed dose, it is necessary to obtain the total number of decays occurring within the target volume. Dose distributions were therefore calculated within cubic matrices consisting of arrays of cubic voxels over which this equation was integrated. The  $^{131}\text{I}$  dose kernel used in this study was that of Telenczak (11). For each voxel within the matrix, the total number of decays occurring within that voxel was determined. This was achieved by numerically integrating over each voxel. Considering this voxel as a source volume of edge  $dl$ , and assuming all decays to be occurring at the center of the voxel, the resultant dose absorbed within this voxel and each of the other voxels within the matrix was determined. For each voxel, the dose contributions obtained from itself and from all other voxels were then summed.

To demonstrate this method of dosimetry, the model is applied here to the data from one patient. In this case, five SPECT scans were obtained after the end of infusion, on days 2, 3, 4, 7 and 9. These were registered to the initial CT scan with accuracies  $\approx 4$  mm (12). To obtain SPECT image data depicting the distribution of activity as accurately as possible, each scan was reconstructed with a ramp filter and deconvolved with a relevant point-spread function. This was obtained by imaging a point source within an Alderson head phantom filled with water, using the same scan parameters as for the patient. The spatial resolution of the system using these scan parameters was determined by measuring the full width at half maximum of the point-spread functions to be  $\approx 3$  cm. At no time in the processing of the SPECT data were the images smoothed. The data were reconstructed into  $3.2 \text{ mm}^3$  voxels over which the decay concentration equation was integrated in order to

**TABLE 1**  
HWHM and HWTM Values of Activity Profiles from SPECT Scans

Time at which scan was acquired (hr)	HWHM (mm)*	HWTM (mm)*
51.3	14.9 ± 0.7	26.2 ± 1.6
75.1	13.9 ± 1.1	25.5 ± 1.7
97.3	14.7 ± 1.1	26.6 ± 1.5
153.9	14.3 ± 0.5	25.5 ± 1.8
202.3	14.9 ± 0.3	†

\* ± 1 s.d.

† The activity on this final scan was too low for the HWTM to be distinguished from the background.

obtain the activity and dose profiles presented here. Similarly, voxels of this size were used for summing the dose to produce the dose-volume histograms, these sizes being comparable to the dimensions used in sampling dose in the case of external beam radiotherapy.

For this patient, an initial activity of 383 MBq was infused through a single catheter over 15.5 hr. The spatio-temporal distribution of activity throughout the course of the scans may be seen from the half width at half maximum (HWHM) and half width at tenth maximum (HWTM) values shown in Table 1. Each value for the HWHM and HWTM is a mean taken from profiles along the  $x$ ,  $y$  and  $z$  axes, passing through the voxel of maximum intensity.

The low values for the standard deviation justify the assumption that diffusion occurs within a homogeneous medium. Furthermore, these values all agree to within 1.1 mm, implying that the uniformity of distribution is temporal as well as spatial. This indicates that diffusion has ceased before the time of the first scan.

From the registered image data it was evident that the effective decay of the isotope occurred in two phases, the first being 25.8 hr and the second being 76.2 hr. The time from which the second phase dominated was 94.4 hr.

Using Equation 37, the HWHM and HWTM values were used to obtain an estimate for the diffusion constant,  $\kappa$ , dependent on the time at which diffusion has ceased,  $t_D$ . Values for  $\kappa$  are given for three values of  $t_D$ , corresponding to the earliest possible time for cessation of diffusion, 16 hr, the time at which the first scan was obtained, 51.3 hr, and for a point in between, 24 hr (Table 2).

It is noticeable that there is a stronger correlation for the value of  $\kappa$  as estimated from both the HWHM and the HWTM for the two earlier values of  $t_D$ . Thus, these values of  $t_D$  were used for the following calculations, with the corresponding mean values of  $\kappa$ , i.e.,  $\kappa = 0.018 \text{ cm}^2\text{h}^{-1}$  and  $\kappa = 0.055 \text{ cm}^2\text{h}^{-1}$ .

### RESULTS

Predicted activity distributions obtained using Equation 27 were directly compared with profiles obtained from the SPECT images (Figs. 2–4). Because the image data did not give absolute values of activity, all profiles were normalized to the

**TABLE 2**  
Diffusion Constant Resulting from Time of Abrupt Cessation of Diffusion,  $t_D$

Time of abrupt cessation of diffusion, $t_D$ (hr)	Value of $\kappa$ based on HWHM ( $\text{cm}^2\text{h}^{-1}$ )	Value of $\kappa$ based on HWTM ( $\text{cm}^2\text{h}^{-1}$ )
51.3	0.019	0.017
24.0	0.059	0.051
16.0	0.523	0.244

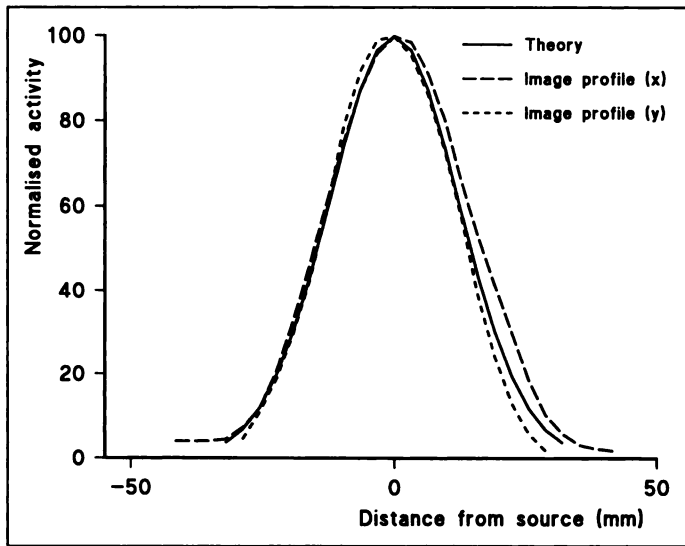


FIGURE 2. Predicted profiles and image profiles of normalized activity corresponding to  $t = 51.3$  hr.

first, which was given a maximum value of 100. Similarly, the predicted profiles were also normalized to that corresponding to the time of the first scan, which is therefore also given a maximum value of 100. In these plots, just one value of  $\kappa$  and  $t_D$  have been plotted, since it has been shown that both sets of values produce similar profiles, and two image profiles (those for  $y, z$ -constant and for  $x, z$ -constant) are shown. The high statistics obtained for the earlier scan have resulted in a smoother image profile than for the 10-day scan where statistical fluctuations are evident.

The spatial resolution of the gamma camera prevents accurate determination of the activity distribution and will depict a greater homogeneity than will actually be the case. Working within the limitations of the modality, however, the above figures show a good agreement between the activity profiles as obtained from the image data and those predicted, justifying Equation 27 and hence Equation 28 as a means of calculating the dose distribution. After convolution of these activity distributions with the relevant point-source dose kernel, the absorbed dose values were binned into voxels and the dose distribution graphically displayed (Fig. 5). The absorbed dose profile is shown in Figure 6.

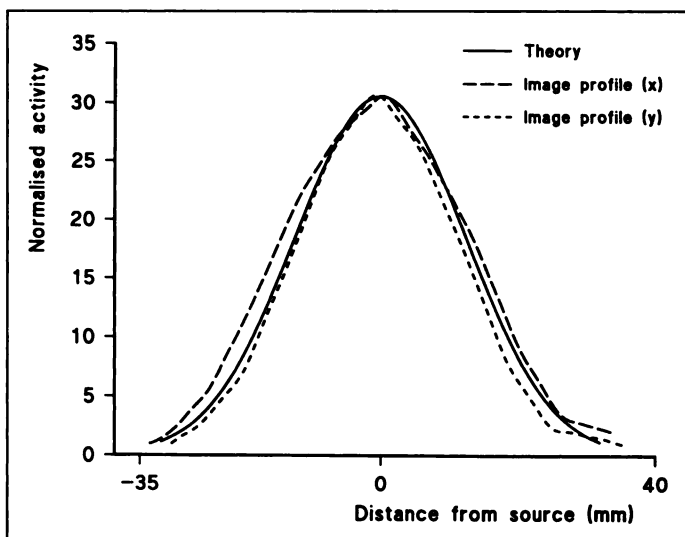


FIGURE 3. Predicted profiles and image profiles of normalized activity corresponding to  $t = 97.3$  hr.

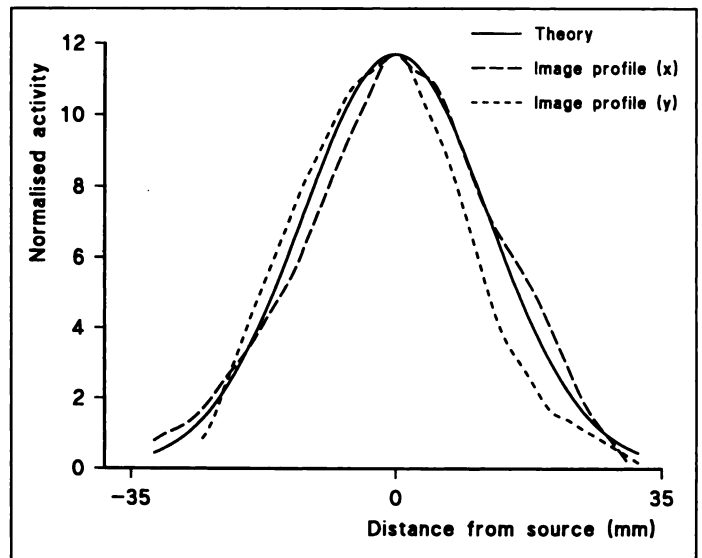


FIGURE 4. Predicted profiles and image profiles of normalized activity corresponding to  $t = 202.3$  hr.

It is clear from this plot that the values  $\kappa = 0.018 \text{ cm}^2\text{h}^{-1}$ ,  $t_D = 51.3$  hr, produce an absorbed dose value close to the source that is greater by a factor of 2.7 than for  $\kappa = 0.055 \text{ cm}^2\text{h}^{-1}$ ,  $t_D = 24$  hr. This factor decreases with distance from the source.

Using these three-dimensional dose distributions, integral DVHs were calculated for both sets of values of  $\kappa$  and  $t_D$  (Fig. 7). In Figure 8 the dose values are windowed to show a maximum of 100 Gy. It is evident from this figure that despite the large discrepancy in maximum dose values seen in Figure 8, the similarity in the dose distribution below 100 Gy results in comparable histograms. The difference between the ideal (whereby 100% of the volume receives 100% of the dose) and the actual DVHs shown here is striking, particularly when compared with results obtained for external-beam radiotherapy.

## DISCUSSION

The results obtained here are only sufficient to draw preliminary conclusions. One point to note however is that in this particular trial the distribution of absorbed dose is more important than the average dose value. Thus, even if the mean

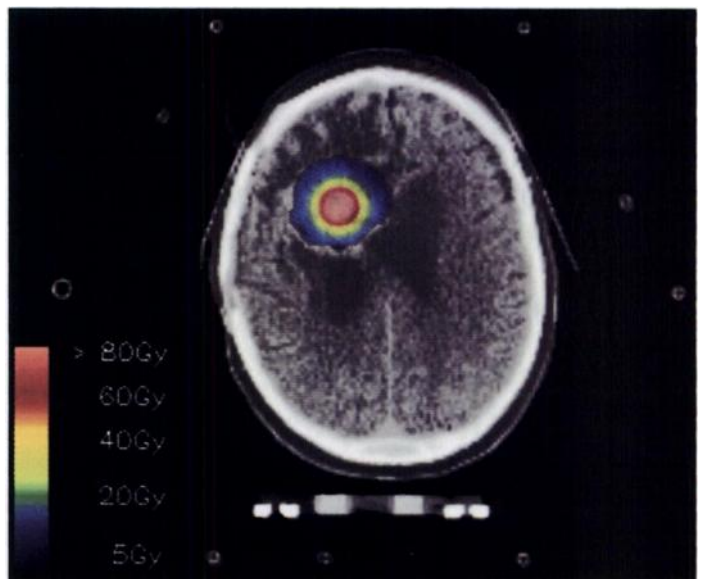


FIGURE 5. Absorbed dose distribution for patient A superimposed onto a registered CT slice.

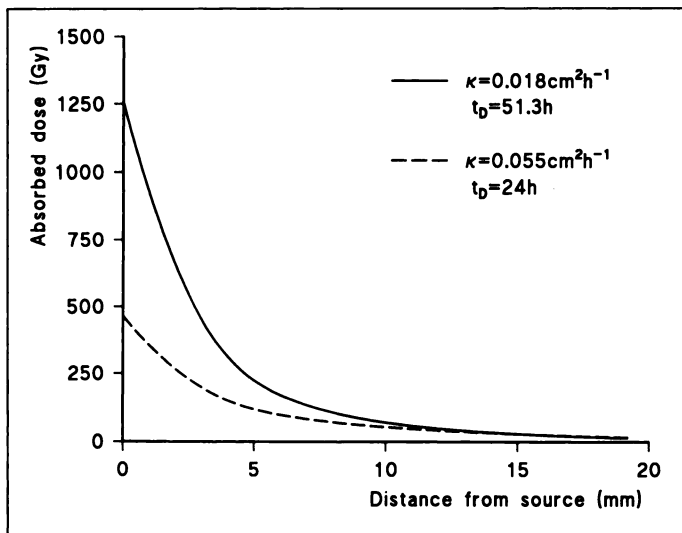


FIGURE 6. Line profiles of absorbed dose distribution.

dose value was largely underestimated, it would still be the case that a large volume of the tumor was underdosed, resulting in the same poor tumor control.

Further investigation is required to validate this model fully. This will include laboratory and phantom work, although it will necessitate the design and construction of a suitable phantom whereby diffusion can occur at a known (and preferably fixed) rate. For future studies more image data should be obtained where possible, particularly at earlier time points.

This method of dosimetry opens up a new possibility for individual patient treatment planning. It should be possible using this method to administer a tracer dose and determine from the measured effective half-life and diffusion coefficient the level of activity that would be required to achieve sufficient therapeutic doses to all parts of the tumor, while minimizing the dose to normal tissue. It will also be possible to determine a priori the likely effect of using different isotopes or antibodies with different diffusion characteristics, as well as the optimum number and placement of catheters.

## CONCLUSION

A novel method of dosimetry has been developed using mathematical modeling and registered image data that may be applied to intravesical radionuclide therapy. Three-dimen-

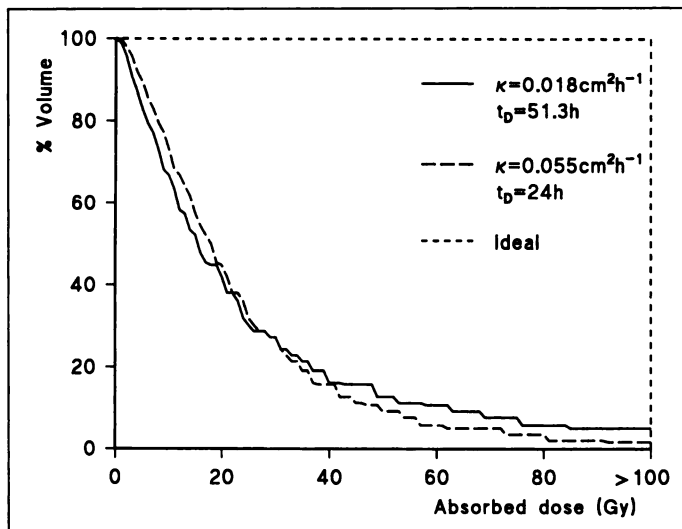


FIGURE 7. Integral dose-volume histogram.

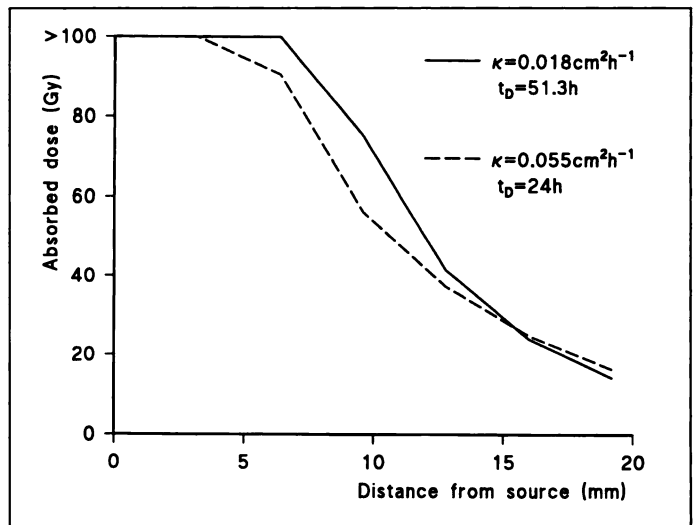


FIGURE 8. Line profiles of absorbed dose distribution with dose windowed to show a maximum of 100 Gy.

sional absorbed dose distributions were obtained that allow for temporal as well as spatial heterogeneity of the distribution of administered activity. This method enabled dose values to be obtained without the need of a calibration scan, which to date has been the only means of quantifying absolute dose. The initial results presented here are promising, although further study is required to validate this method fully.

## ACKNOWLEDGMENT

The work of the Joint Department of Physics is supported by the Cancer Research Campaign.

## REFERENCES

- Zalutsky M, Moseley P, Coakam HB, Coleman RE, Bigner D. Pharmacokinetics and tumour localization of  $^{131}\text{I}$ -labeled anti-tenascin monoclonal antibody 81C6 in patients with glioma and other intracranial malignancies. *Cancer Res* 1989;49:2807-2813.
- Loevinger R, Berman M. A revised scheme for calculating the absorbed dose from biologically distributed radionuclides. *MIRD pamphlet No. 1*, revised. New York, NY: Society of Nuclear Medicine; 1976.
- Chittenden S, Thomas R, Hall A, et al. Dosimetry of intravesical  $^{131}\text{I}$ -monoclonal antibody (MAb) therapy in patients with recurrent high-grade gliomas: radioactive isotopes in clinical medicine research. In: *Radioactive isotopes in clinical medical research. Advances in pharmacological sciences*. Basel, Switzerland: Birkhauser Verlag; 1995:29-34.
- Webb S, Nahum AE. A model for calculating tumor-control probability in radiotherapy including the effects of inhomogeneous distributions of dose and clonogenic-cell density. *Phys Med Biol* 1993;38:653-666.
- Sgouros G, Barest G, Thekkumthala J, et al. Treatment planning for internal radionuclide therapy: three-dimensional dosimetry for nonuniformly distributed radionuclides. *J Nucl Med* 1990;31:1884-1891.
- Sgouros G, Chui S, Pentlow KS, et al. Three-dimensional dosimetry for radioimmunotherapy treatment planning. *J Nucl Med* 1993;34:1595-1601.
- Ogawa K, Kanbe N, Uchida I, Yamada Y, Itoh A, Akiyama Y. Accurate three-dimensional dose calculation using a quantitative SPECT image for radioimmunotherapy [Abstract]. *J Nucl Med* 1994;35(suppl):160P.
- Giap HB, Macey DJ, Bayouth JE, Boyer AL. Validation of a dose-point kernel convolution technique for internal dosimetry. *Phys Med Biol* 1990;40:365-381.
- Crank J. *The mathematics of diffusion*. London: Oxford University Press; 1967.
- Fielding SL, Flower MA, Ackery D, Kemshead JT, Lashford LS, Lewis I. Dosimetry of iodine-131 metaiodobenzylguanidine for treatment of resistant neuroblastoma: results of a UK study. *Eur J Nucl Med* 1991;18:308-316.
- Telenczak P. Apport de la microscopie ionique analytique et des methodes de Monte Carlo (EGS4-Presta) pour l'optimisation des parametres dosimetriques en radiotherapie metabolique [Doctoral thesis No. 846]. Toulouse, France: Universite Paul Sabatier; 1991.
- Flux GD. Multimodality image registration and its application to the dosimetry of intravesical radionuclide therapy [PhD thesis]. London, England: University of London; 1995.